From amyloid fibrils to microfiber condensates: Tuning microfluidic coextrusion of food-grade β-lactoglobulin-pectin core-shell fibers by changes of protein structure

Journal Article

Author(s):
Kutzli, Ines; Lutz Bueno, Viviane; Bagnani, Massimo; Diaz, Ana; Almohammadi, Hamed; Nicholson, Reed A.; Baier, Stefan K.; Mezzenga, Raffaele

Publication date:
2023-10

Permanent link:
https://doi.org/10.3929/ethz-b-000615027

Originally published in:
Food Hydrocolloids 143, https://doi.org/10.1016/j.foodhyd.2023.108845

Food Hydrocolloids 143 (2023) 108845

Contents lists available at ScienceDirect

Food Hydrocolloids

journal homepage: www.elsevier.com/locate/foodhyd

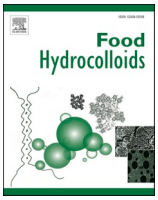

From amyloid fibrils to microfiber condensates: Tuning microfluidic coextrusion of food-grade β-lactoglobulin-pectin core-shell fibers by changes of protein structure

Ines Kutzli [a], Viviane Lutz-Bueno [a,b], Massimo Bagnani [a], Ana Diaz [b], Hamed Almohammadi [a], Reed A. Nicholson [c], Stefan K. Baier [c,d], Raffaele Mezzenga [a,e,*]

[a] Institute of Food, Nutrition and Health (IFNH), Department of Health Sciences and Technology (HEST), ETH Zurich, 8092, Zurich, Switzerland
[b] Paul Scherrer Institute, 5232, Villigen PSI, Switzerland
[c] Motif FoodWorks, Inc., 27 Drydock Ave, Boston, MA, 02210, USA
[d] School of Chemical Engineering, The University of Queensland, Brisbane, QLD, 4072, Australia
[e] Department of Materials, ETH Zurich, 8093, Zurich, Switzerland

ARTICLE INFO

Keywords:
Microfluidic spinning
Protein nanofibrils
Wide-angle X-ray scattering
Hierarchical assembly
Mechanical properties
Structural orientation

ABSTRACT

Protein-based microfibers have potential applications in bioengineering and food but preserving and utilizing the unique nanomechanical properties of their protein building blocks at the micrometer scale remains a challenge. This study investigates the bottom-up fabrication of core-shell fibers by coaxial microfluidic spinning of pectin and β-lactoglobulin in different conformational states (monomeric, amyloid fibrils, shortened amyloid fibrils in their isotropic/nematic phases), gelled in $CaCl_2$ solution. Fiber diameters ranged between 478 and 855 μm (wet state) and 107–135 μm (dry state). They showed clear core-shell cross-sections, except pectin-β-lactoglobulin monomer fibers where the compact protein is presumably understood to diffuse through the pectin matrix. The molecular orientation of the fiber building blocks was expressed as order parameters representing the alignment of pectin chains and amyloid fibrils parallel to the fiber axis calculated from synchrotron wide-angle X-ray scattering (WAXS) with a spatial resolution of 20 μm. Introduction of amyloid fibrils as the protein core increased the Young's modulus from 3.3 to 6.4 GPa and tensile strength from 117 to 182 MPa compared to pure pectin fibers. Increasing the protein core flow rate from 1 to 2 mL/h, however, caused helical bending of the core jet, a decrease in order, and ultimately worsened mechanical performance. Overall, full length amyloid fibrils proved to be more beneficial to the mechanical properties than shortened amyloid fibrils. By providing insight into the relationship between protein conformation, spinning flow rate, and resulting mechanical properties of core-shell microfibers, these results may contribute to the field of novel fibrous protein-based materials.

1. Introduction

Hydrogels can be spun into fibrous materials at the micro- or nano-scale. These hydrogel fibers are an attractive material for widespread applications in the fields of tissue engineering (Jun et al., 2014; Nemati et al., 2019), drug encapsulation and delivery (Hu et al., 2014; Kumar et al., 2019; Sharifi et al., 2016; Singh et al., 2021), sensing technologies (Yu et al., 2017; Zhou et al., 2018), and food science (Chen et al., 2021; Cui et al., 2022; Kutzli et al., 2019), due to their outstanding properties such as their large surface-to-volume ratio that allows for fast matter exchange or their increased mechanical strength compared to the bulk hydrogel.

Fiber fabrication techniques include wet spinning, dry spinning, electrospinning, microfluidic spinning, direct drawing, and direct writing (Shang et al., 2019). In the past, fibers from food-grade proteins, e.g., soy protein (Huang et al., 1995; Liu et al., 2017), peanut protein (Fletcher & Ahmed, 1977), pea and fava bean proteins (Gallant et al., 1984), and casein (Burgess & Downey, 1979; Downey & Burgess, 1979) were mainly manufactured using wet spinning processes. The proteins lose their native structure in the process and rather exist in an unordered, denatured state (Mu et al., 2019; Zhang et al., 2003). Recently, microfluidic spinning has opened the possibility to generate food-grade fibers from polysaccharides and/or proteins with great design flexibility

* Corresponding author. Institute of Food, Nutrition and Health (IFNH), Department of Health Sciences and Technology (HEST), ETH Zurich, 8092, Zurich, Switzerland.
E-mail address: raffaele.mezzenga@hest.ethz.ch (R. Mezzenga).

https://doi.org/10.1016/j.foodhyd.2023.108845
Received 21 March 2023; Received in revised form 19 April 2023; Accepted 30 April 2023
Available online 12 May 2023

under relatively mild conditions at ambient temperature without organic solvents or chemical cross-linkers as oftentimes required for wet spinning (Chen, Jones, & Campanella, 2021; Sun et al., 2021). By allowing the precise manipulation of multiphase flows at the micron scale, microfluidic spinning is an outstanding tool to generate complex multicomponent biomaterials such as core-shell fibers, offering possibilities to tailor fiber properties to the intended application (Du et al., 2019; Wang et al., 2022). The high functionality of these materials arises from the hierarchical self-assembly of their building blocks into highly organized structures at multiple length scales (Ye et al., 2022). However, it remains challenging to develop high-performance fibers at the micrometer length scale from protein building blocks with well-defined quaternary structures, while at the same time retaining their outstanding mechanical properties at the nanoscale (Meier & Welland, 2011; Wegst et al., 2015).

An example for highly ordered protein building blocks is amyloid protein nanofibrils (PNF). They can self-assemble *in vitro* from a wide range of proteins under specific conditions, namely low pH at elevated temperatures, where the proteins get partially unfolded or hydrolyzed (Cao & Mezzenga, 2019; Li et al., 2023). The peptide building blocks then form fibrils with a high aspect ratio via intermolecular stacking of β-sheets (Knowles & Mezzenga, 2016). A well-studied example is the milk protein β-lactoglobulin (BLG) (Adamcik et al., 2010; Bolisetty et al., 2011).

Furthermore, manipulating these fibrillar structures, such as shortening the contour length, leads to self-assembly by nucleation and growth of liquid crystalline droplets at a protein concentration where isotropic and nematic phases coexist (Nyström et al., 2018). As opposed to the isotropic continuous phase without long-range positional order, the emerged microdroplets – so called tactoids – show directional order along their axis. They are therefore birefringent and visually detectable with cross-polarized filters (He et al., 2016). A promising approach for the design of new materials is the manipulation of tactoid shape by microfluidics (Almohammadi et al., 2020). Embedding amyloid fibrils in their isotropic and nematic phases into other matrices to produce hybrid materials has not yet been explored. A critical difference between the two phases is that amyloid fibrils in the nematic phase are supposed to be already highly ordered once injected for microfluidic fiber production, whereas amyloid fibrils in the isotropic phase are randomly oriented during injection. This could have an effect on the structural orientation in the resulting fibers that might be therefore characterized by different mechanical properties.

So far, full length BLG nanofibrils have been structured into functional macroscale materials, such as hydro- and aerogels (Cao et al., 2018; Peydayesh et al., 2020; Usuelli et al., 2021) or films (Peydayesh et al., 2021). They have also been successfully spun into microfibers by complex coacervation with gellan gum (Meier & Welland, 2011), by gelling them with acetate buffer in a double flow-focusing device (Kamada et al., 2017), by blending and gelling them with alginate in a microfluidic channel (Kamada et al., 2020), by dry spinning them with gelatin (Lutz-Bueno et al., 2020), and by cross-linking them with genipin in a flow-focusing channel (Ye et al., 2022). However, multicomponent core-shell fiber systems remain to be investigated. Core-shell fibers consist of two separate compartments, the outer shell and the inner core, and combine the mechanical, physical or chemical properties of two or more different materials.

This work aims at exploring the formation and properties of food-grade core-shell fibers with a spatially divided protein core and a polysaccharide shell. A one-step coaxial microfluidic spinning process was used to fabricate core-shell fibers using BLG as the core material and low methoxyl pectin, gelled by calcium cations (Ca^{2+}), as the shell material. A previous study demonstrated that the morphology of protein nanofibrils alters the mechanical properties of fibers spun thereof (Kamada et al., 2017). To further explore the potential of tunable mechanical properties, BLG in monomeric state, BLG amyloid fibrils, or shortened BLG amyloid fibrils in their isotropic/nematic phases were chosen as core flow. To better understand the alignment and orientation process of BLG in different conformational states, the flow rates of the spinning process were altered. The alignment and composition distribution inside the fibers was investigated using wide angle X-ray scattering (WAXS) with a micrometric beam size, which could scan at multiple positions through the cross-section of the core-shell fibers, taking into account their multiphasic design. Furthermore, fiber morphology was analyzed by scanning electron microscopy (SEM) and confocal laser scanning microscopy (CLSM). Fiber mechanical properties were evaluated by tensile testing.

2. Materials and methods

2.1. Materials

Whey protein isolate (WPI, batch number 22895316) was provided by Fonterra (Auckland, New Zealand) and low methoxyl (LM) pectin with a degree of esterification (DE) of 35% (Classic AU-L 101/20, lot number 02010032) was kindly provided by Herbstreith & Fox GmbH & Co. KG (Neuenbürg, Germany). Hydrochloric acid (HCl, 37%) was purchased from VWR International GmbH (Dietikon, Switzerland). $CaCl_2$ dihydrate (≥99.0%), phenol red, polyethylene glycol (average M_n 35,000 Da), sodium alginate, thioflavin T, and other chemicals used were all obtained from Sigma-Aldrich/Merck AG (Buchs, Switzerland).

2.2. Preparation and characterization of β-lactoglobulin solutions

2.2.1. Monomer solution

The monomer (mono) solution was prepared from β-lactoglobulin (BLG) purified from WPI according to Vigolo et al. (2017). BLG was dissolved at 2% w/w in Milli-Q water and filtered through a 0.45 μm nylon syringe filter before the pH was adjusted to 2 with HCl.

2.2.2. Amyloid fibrils solution

To obtain BLG amyloid fibrils (AF), a solution of BLG monomer (2% w/w in Milli-Q water, filtered through a 0.45 μm nylon syringe filter, pH 2) was incubated at 90 °C in an oil bath for 5 h while continuously stirring at 300 rpm.

2.2.3. Isotropic and nematic phase

Once BLG amyloid fibrils (BLG AF) were prepared, the method of Nyström et al. (2018) was applied to initiate phase separation into isotropic phase (IP) and nematic phase (NP). Briefly, an immersion blender (Beper S.r.l., Vallese, Italy) on speed setting 2 was used to shorten the fibrils with mechanical shear force. To remove unreacted monomers and peptides, the solution was dialyzed with 100 kDa MWCO membranes (SpectraPor, Repligen, Waltham, MA, USA) against Milli-Q water, pH 2, for 5 days with daily water exchange. Afterwards, the solution was upconcentrated using 6–8 kDa MWCO dialysis membranes (SpectraPor, Repligen, Waltham, MA, USA) against a polyethylene glycol (PEG, average M_n 35,000 Da) solution (6% w/w, pH 2) in order to reach a protein concentration where isotropic and nematic phases coexist. The solution was stored at 4 °C until complete macroscopic separation into isotropic and nematic phases occurred (see Supplementary data Fig. S1 A). The BLG concentration of the isotropic (2.35 ± 0.04% w/w) and the nematic (2.92 ± 0.03% w/w) phases were determined gravimetrically in triple determination. The formation and morphology of tactoids in the nematic phase was checked using a light microscope (Axio Scope.A1, Carl Zeiss AG, Jena, Germany) with polarization filters (see Supplementary data Fig. S1 B).

2.2.4. AFM

Atomic force microscopy (AFM) was used to characterize the morphology distributions of amyloid fibrils right after incubation and after shortening, both in the isotropic and nematic phases. Small aliquots of the samples (10 μL) were diluted with pH 2 Milli-Q water down

to a concentration of 0.02% w/w. 20 μL of the diluted samples were deposited onto freshly cleaved mica, incubated for 1 min, rinsed with 1 mL pH 2 Milli-Q water, and dried with gentle air flow. Imaging was performed in air and ambient conditions, using a Multimode VIII scanning probe microscope in tapping mode (Bruker, Billerica, MA, USA). The length and height distributions of the fibrils were characterized by analyzing the acquired images using the open source software FiberApp (Usov & Mezzenga, 2015).

2.3. Electrophoretic mobility

The ζ-potential of BLG and pectin solutions was determined using a particle electrophoresis instrument (Nano ZS, Malvern Instruments, Malvern, UK) at 25 °C. The ζ-potential was calculated with the Smoluchowski equation. Measurements were carried out in duplicate.

2.4. Microfluidic spinning

The spinning process of core-shell hydrocolloid-BLG fibers was performed with a microfluidic device consisting of two coaxially aligned borosilicate glass capillaries. A round capillary (d_{inner} = 0.6 mm, d_{outer} = 1.0 mm) with a tapered orifice (d_{inner} = 0.1 mm) was aligned and fixed in the middle of a square capillary (d_{inner} = 1.05 mm) on a glass slide with UV-curable glue. Due to the matching inner/outer dimensions of the two capillaries, precise axis alignment was ensured. The distance from the tip of the inner capillary to the outlet of the outer capillary was 15 mm. The ends of the capillaries were connected to luer stubs (d_{inner} = 0.34 mm, d_{outer} = 0.64 mm). The luer stubs were connected to syringes with flexible tubing (d_{inner} = 0.8 mm). The microfluidic spinning process in the capillary microfluidic device was observed with a light microscope equipped with a camera (Axio Scope.A1, Carl Zeiss AG, Jena, Germany).

The double coaxial spinning of fibers containing two different core materials was performed with a similar device. Another round capillary (d_{inner} = 0.2 mm, d_{outer} = 0.4 mm) with a tip (d_{inner} = 0.05 mm) was inserted into the round capillary and aligned in the center. The tip of the innermost capillary had a distance of 35 mm to the tip of the wider round capillary.

The spinning of pure hydrocolloid fibers was performed with a microfluidic device consisting of a square capillary (see Fig. 1 for schematic drawings and Supplementary data Fig. S2 for images of the microfluidic devices).

Pure hydrocolloid fibers were produced from a solution of low methoxyl (LM) pectin (0.85% w/w, pH 2). Pectin was dissolved in Milli-Q water at a concentration of 1% w/w. The pH was adjusted to 2 with HCl. The solution was centrifuged (10,000 rpm, 15 min) to remove air bubbles and undissolved particles. The solution was pumped through the capillary with flow rates of 5 or 10 mL/h, respectively, using a syringe pump (PHD2000, Harvard Apparatus, Holliston, MA, USA). Gelation was achieved by directing the flow at the outlet of the capillary into a 20% w/w $CaCl_2$ solution. Alginate fibers were spun from a 1.5% w/w solution of alginate with the same setup and gelled in a 0.1 M $CaCl_2$ solution.

Fibers with a BLG protein core and a hydrocolloid shell were produced by first introducing the protein solution of either BLG monomer (mono), BLG amyloid fibrils (AF) or BLG isotropic phase amyloid fibrils (AF-IP) into the inner capillary with a syringe pump at 1 or 2 mL/h immediately followed by the shell stream of pectin (or alginate) through the outer capillary at 10 mL/h by a second syringe pump. Fibers were gelled and collected at the outlet in a 20% w/w $CaCl_2$ solution.

Flow rates of double coaxial spinning of pectin-BLG fibers, where the inner core stream was BLG nematic phase amyloid fibrils (AF-NP), the outer core stream was BLG isotropic phase amyloid fibrils (AF-IP), and the shell stream was pectin, were 0.1 mL/min for BLG AF-NP, 2 mL/h for BLG AF-IP, and 10 mL/min for pectin.

All fibers were washed with Milli-Q water and stored in 0.1 M $CaCl_2$ at 4 °C for further analysis.

2.5. Fiber morphology

2.5.1. Fiber diameter

Fiber diameters of wet as-spun fibers and of air-dried (24 °C, 50% relative humidity, 72 h) fibers were measured using light micrographs (Axio Scope.A1, Carl Zeiss AG, Jena, Germany). Fiber diameters were obtained from at least 30 measurements for each sample by image analysis using ImageJ (Schneider et al., 2012). A one-way analysis of variance (ANOVA) with a subsequent Tukey's test was performed in OriginPro 2021 (OriginLab, Northampton, MA, USA). Significant

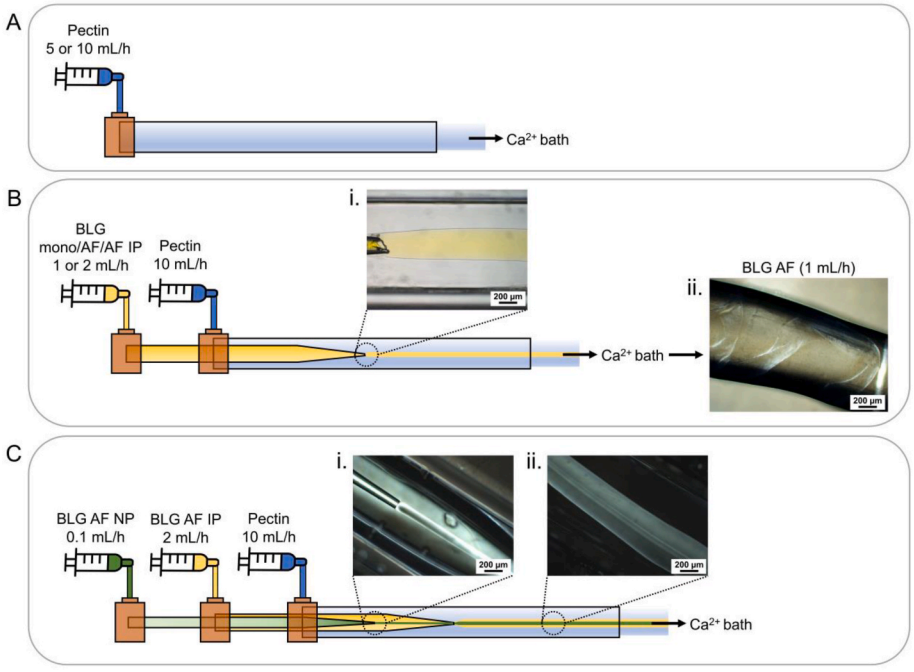

Fig. 1. Schematic illustration of the capillary microfluidic setups including the flow rates used for A: spinning of solid pectin fibers; B: coaxial spinning of pectin-BLG fibers with a core stream of either BLG monomer (mono), BLG amyloid fibrils (AF) or BLG isotropic phase amyloid fibrils (AF-IP), and a pectin shell stream. Light (i.) and polarized light (ii.) optical micrographs show the generation of a cylindrical core jet in the capillary during spinning and the coiled morphology of the BLG AF fiber core in the final fiber in wet state; C: double coaxial spinning of pectin-BLG fibers with an inner core stream of BLG nematic phase amyloid fibrils (AF-NP), an outer core stream of BLG isotropic phase amyloid fibrils (AF-IP), and a pectin shell stream. Polarized light optical micrographs (i. and ii.) show the generation of two cylindrical core jets in the capillaries during spinning. The pectin shell gels in a $CaCl_2$ bath at the outlet of the microfluidic setups, respectively.

differences ($p < 0.05$) were labeled with different letters.

2.5.2. Scanning electron microscopy (SEM)

Fibers were prepared for scanning electron microscopy (SEM) in a PELCO BioWave, Pro + microwave system (Ted Pella, Redding, CA, USA), following a microwave-assisted fixation and dehydration procedure. Fixation was done in 3% glutaraldehyde/2% paraformaldehyde in 0.1 M $CaCl_2$ on ice. After washing in $CaCl_2$, samples were postfixed in 1% OsO_4 in water (bidistilled), washed again (bidistilled water) and dehydrated in a graded series of ethanol (50%, 75%, 90%, 98%, and three times 100%) on ice followed by critical point drying out of dry ethanol (CPD 931, Tousimis, Rockville, MD, USA). The resulting samples were mounted on SEM aluminum stubs and vertically in conductive carbon paint for cross-sections and then rotary sputter-coated with 6 nm of platinum/palladium. Samples were observed with a SU5000 (Hitachi, Chiyoda, Japan) under high vacuum operated at an acceleration voltage of 2 kV at 6–7 mm working distance.

2.5.3. Confocal laser scanning microscopy (CLSM)

Fibers were immersed in 100 μM thioflavin T (ThT) solution for 1 h before being rinsed extensively with Milli-Q water. The wet fibers were imaged with a confocal laser scanning microscope (SP8 STED, Leica Microsystems GmbH, Wetzlar, Germany). The excitation wavelength used was 473 nm. Sample emission was collected at 480–585 nm.

2.6. Fiber composition

2.6.1. Dry matter

The dry matter content was measured gravimetrically in triplicate by drying fiber samples in an oven (60 °C, 48 h).

2.6.2. Protein content

The nitrogen content of freeze-dried fibers was determined by micro-elemental combustion analysis using a LECO TruSpec Micro (Leco Instrumente GmbH, Mönchengladbach, Germany). The protein content expressed on a dry matter basis was calculated from the nitrogen content using a conversion factor of 6.25. Due to the limited sample amount for some fibers, protein content was either determined in single or double determination.

2.7. Wide angle X-ray scattering (WAXS)

Air-dried (24 °C, 50% relative humidity, 72 h) fibers were mounted on a sample holder (see Supplementary data Fig. S3). Synchrotron WAXS measurements were performed at the cSAXS beamline of the Swiss Light Source (SLS) Paul Scherrer Institute (PSI) (Villigen, Switzerland) at a wavelength of 1 Å. The X-ray beam was focused on the sample to 51 × 17 μm^2 and shined perpendicularly to the axis of the fibers. The fiber was moved vertically in front of the beam with a step size of 20 μm. For example, a fiber with a thickness of 100 μm leads to 5 scattering patterns, collected along the cross-section. WAXS patterns were recorded with a Pilatus 2M detector with pixel size 172 μm placed at a distance of 0.236 m from the sample in air without any flight tube in between. The WAXS measurement intensity was corrected by the transmission, which is collected by the beam stopper diode during small angle X-ray scattering (SAXS) of the same samples and corrected for sample thickness. Each WAXS measurement point was a single detector acquisition with an exposure time of 0.1 s.

The 2D scattering patterns were radially integrated into 1D curves of scattering intensity as a function of scattering vector (q). The 2D scattering patterns were also azimuthally integrated into 1D curves of the scattered intensity as a function of azimuthal angle (χ), as shown in Fig. 3A iii, revealing the positions in q of the intensity peaks at 8 $Å^{-1}$ (P1), 13 $Å^{-1}$ (P2), and 15 $Å^{-1}$ (P3). All the codes used for the data reduction were developed by the Coherent X-ray Scattering group at the PSI and can be found on the cSAXS web page at https://www.psi.ch/sls/csaxs/software.

Molecular alignment in the fibers is assessed by the orientation order parameter (S), calculated based on the radially integrated intensity in the q-ranges at 8 $Å^{-1}$ (P1) for S_{P1}, 13 $Å^{-1}$ (P2) for S_{P2}, and 15 $Å^{-1}$ (P3) for S_{P3} as a function of the azimuthal angle (χ), as shown in Fig. 3A iv. The rings were integrated ± 5 pixels from these q positions in order to extract the anisotropy of the sharp peaks.

$$S = \frac{3\langle \cos^2 \chi \rangle - 1}{2}$$

The final S then is calculated employing the following average (Ward, 2012):

$$\langle \cos^2 \chi \rangle = \frac{\int_0^{\pi} I(q,\chi) \cos^2 \chi \sin \chi d\chi}{\int_0^{\pi} I(q,\chi) \sin \chi d\chi}$$

To calculate a smooth order parameter, the gaps between the moduli of the Pilatus 2M detector were removed. This correction applied a radial replacement filter, and the gaps of the detector were replaced with counts, considering the symmetry condition of the scattering pattern. In this work, we show only the corrected 2D scattering patterns in linear scale, thus notice the absence of detector gaps towards the center of the pattern, where valid data was available to fill these gaps.

2.8. Mechanical properties

Tensile mechanical testing of the dried fibers at ambient conditions was performed on a Z010 (ZwickRoell, Ulm, Germany) equipped with clamps and a 10 N load cell. Air-dried (24 °C, 50% relative humidity, 72 h) fibers were fixed to a paper slip with a 5 mm gap using UV-curable glue. The diameter of each fiber specimen was measured with an optical microscope and used to calculate the tensile stress. The paper slips were mounted in the clamps of the machine and the paper was cut before applying uniaxial tension to the samples at a constant rate of 5 mm/min. For each fiber composition, 5–7 specimens were tested. Young's modulus, ultimate tensile strength, and elongation at break were calculated from the recorded stress-strain curves. A one-way analysis of variance (ANOVA) with a subsequent Tukey's test was performed in OriginPro 2021 (OriginLab, Northampton, MA, USA). Significant differences ($p < 0.05$) were labeled with different letters.

3. Results and discussion

3.1. Microfluidic spinning process

Microfluidic spinning was carried out using a geometry composed of coaxial glass capillaries. For pure pectin fibers, just one capillary was used (Fig. 1 A). For core-shell fibers, pectin solution was flowing through the outer capillary as the shell flow and protein solution containing BLG in different conformational states was pumped through the inner capillary/capillaries (Fig. 1 B and C). The coaxial flow was directed into a $CaCl_2$ bath at the capillary outlet to cross-link the pectin shell. The gelation process of the low methoxyl pectin shell in the $CaCl_2$ bath is fast occurring and driven by the ionic interactions of blocks of 6–20 de-esterified galacturonic acid residues from the smooth regions of the pectin backbone with divalent ions such as Ca^{2+} (Cao et al., 2020). The structure of such a junction zone is generally described with the so-called "egg-box" model.

For stable continuous fiber production, pectin was injected at 10 mL/h into the outer capillary and BLG mono/AF/AF-IP was injected at either 1 or 2 mL/h into the inner capillary. The interface of the solutions of pectin and BLG could be observed during spinning under a light microscope (Fig. 1 B i). In the case of double coaxial spinning with BLG AF-NP as the inner core, BLG AF-IP as the outer core, and pectin as the shell, the interface between the nematic and the isotropic phases of BLG could be observed using polarized light microscopy due to the birefringence of

the amyloid fibrils under shear (Fig. 1 C i and ii).

Although the inner and the outer jets appeared to be parallel at the outlet of the inner tapered capillary, downstream from the outlet and in the spun fibers, the BLG core phase had a wavy morphology. This instability is exemplarily depicted in Fig. 1 B ii for fibers with a BLG AF core (1 mL/h). This buckling instability was ascribed to the so-called "liquid rope-coil effect". Similar to the formation of periodic coiling patterns of thin streams of viscous liquid falling onto surfaces under gravity, liquid streams in a fluid can form coils depending on the flow rates and viscosities (Ribe et al., 2012; Tottori & Takeuchi, 2015). In microfluidics, the coiling phenomenon is triggered by slowing down the viscous liquid stream by injecting it into a less-viscous surrounding sheath fluid (Nie & Takeuchi, 2017).

In the case of $CaCl_2$-induced gelation of alginate, the interface between the outer flow of $CaCl_2$ solution and the inner alginate jet gels instantaneously upon contact. An unbalanced fluid friction between this highly viscous layer and the surrounding fluid subsequently leads to spiraling of the consecutively gelling alginate jet (Liu et al., 2020; Yu et al., 2017).

When the outer flow rate is sufficiently greater than the inner flow rate, the inner jet must be stretched to become straight. However, as the ratio of the flow rates Q_{inner}/Q_{outer} increases (by increasing the flow rate of the inner phase), the inner jet starts to deform (Xu et al., 2017; Yu et al., 2017).

In the case of pectin-BLG fibers, it was hypothesized that the remaining electrostatic interactions at the interface between the positively charged protein (ζ-potential of 26–31 mV at pH 2) and the slightly negatively charged pectin (ζ-potential of -3.8 mV at pH 2) may have led to the formation of complex coacervates – stable macromolecular complexes – that might have increased the local viscosity (for full ζ-potential data see Supplementary data Table S1). Hence, the increased fluid friction might have caused waves in the flow of the BLG core jet. The same structure was observed for alginate-BLG fibers (see Chapter 3.6 and Fig. 5 for discussion). Rope coiling effects increased with the increase of the inner flow rate from 1 to 2 mL/h, consequently increasing the ratio of Q_{inner}/Q_{outer}. Implications on the molecular orientation in the fibers and their mechanical properties are further discussed in Chapter 3.4 and 3.5.

3.2. Fiber composition

The dry matter of the fibers ranged from 0.8% w/w to 2.2% w/w (Table 1). Pure pectin fibers had a dry matter content of 1.3% w/w. This rather low solid content illustrates the water holding capacity of apple pectin (~10 g water/g (Moll et al., 2022)). For core-shell fibers, the dry matter increased with increasing the flow rate of the protein core from 1 to 2 mL/h – most likely due to the increased amount of protein flowing through the inner capillary at the same extrusion time.

In the case of BLG monomer, the protein content stayed at 1.5% w/w independent of the core flow rate. The protein content of these samples was also noticeably lower than the protein content of the other samples, although all BLG spinning solutions had a similar protein content of 2.0–2.9% w/w (see Chapter 2.6.2). It was hypothesized that the BLG monomer molecules might have diffused through the pectin shell out of the fibers. This explanation seems feasible since no chemical cross-linking of the protein took place during the spinning process and hence the BLG monomer – being globular and much more compact than the linear amyloid fibrils – might have diffused into the surrounding solution driven by osmotic pressure. Furthermore, the attracting negative charges of the pectin shell were widely shielded by Ca^{2+} ions after gelation and did exert only limited electrostatic attraction on the positively charged BLG. The low content of BLG monomer in the fibers is in line with SEM micrographs (Fig. 2 B) where no protein core was observable for these samples (for further discussion see Chapter 3.3, for FTIR analysis see Supplementary data).

For samples with BLG AF and BLG AF-IP, the protein content of the fibers increased from 8.9% w/w to 11.3% w/w and from 9.3% w/w to 16.4% w/w, respectively, with an increased protein flow rate (Table 1). This increase agrees with a study on electrospun core-shell structured fibers with bovine serum albumin-containing dextran as the core where it was shown that the fiber protein content increased with increasing flow rate of the protein-containing core (Jiang et al., 2006).

3.3. Fiber morphology

Samples for SEM were gently fixed and dehydrated using a protocol that preserved the structural information and diameters of the wet state of the fibers (see Chapter 2.5.2).

Side-view SEM micrographs of the fibers show a rather smooth surface with occasional ripples caused by the edge of the glass capillary outlet immersed in the $CaCl_2$ bath (Fig. 2).

The cross-section of the pure pectin fibers was uniform (Fig. 2 A). The fiber containing BLG monomer as the core material had no clear core-shell morphology (Fig. 2 B). Instead, there appeared to be a hollow cavity on the cross-section where a protein core might have been located. This observation is in line with the low protein content of BLG monomer fibers (Table 1) and the theory that globular BLG monomer molecules diffused out of the core and through the pectin shell. Only a low amount of residual protein is trapped within the pectin matrix (for further discussion see Chapter 3.2).

Clear core-shell morphologies were visible for the cross-section micrographs of fibers spun coaxially from pectin with BLG amyloid fibrils (AF), BLG isotropic phase amyloid fibrils (AF-IP), and BLG nematic phase amyloid fibrils inside BLG isotropic phase amyloid fibrils (AF-IP/

Table 1
Influence of composition and spinning flow rates on fiber dry matter (n = 3), fiber protein content on a dry matter basis (n = 1 or 2), and fiber diameters in wet state and dry state (n = 30). Results are expressed as the mean ± standard deviation if applicable. Different superscript letters indicate statistically significant differences between the samples ($p < 0.05$) if applicable.

	Flow rate	Dry matter	Protein content	Diameter wet fiber	Diameter dry fiber
	mL/h	% w/w	% w/w (dry matter)	μm	μm
Pectin	10	1.26 ± 0.18	-	766 ± 71^{b}	125 ± 39^{abc}
+ BLG monomer (monomer)	1	0.84 ± 0.03	1.50*	584 ± 137^{d}	107 ± 37^{c}
	2	1.13 ± 0.17	1.50**	478 ± 96^{f}	114 ± 50^{c}
+ BLG amyloid fibrils (AF)	1	1.37 ± 0.06	8.91 ± 0.03	855 ± 74^{a}	116 ± 36^{bc}
	2	1.49 ± 0.25	11.31*	519 ± 65^{ef}	110 ± 41^{c}
+ BLG amyloid fibrils isotropic phase (AF-IP)	1	1.64 ± 0.17	9.31 ± 0.06	657 ± 102^{c}	116 ± 26^{bc}
	2	2.20 ± 0.07	16.44 ± 0.19	576 ± 78^{de}	124 ± 43^{abc}
+ BLG amyloid fibrils isotropic phase (AF-IP)/nematic phase (AF-NP)	2/0.1	1.99 ± 0.04	n.d.***	478 ± 68^{f}	135 ± 66^{ab}

* Single determination due to limited sample amount.
** Standard deviation equals zero.
*** Not determined due to limited sample amount.

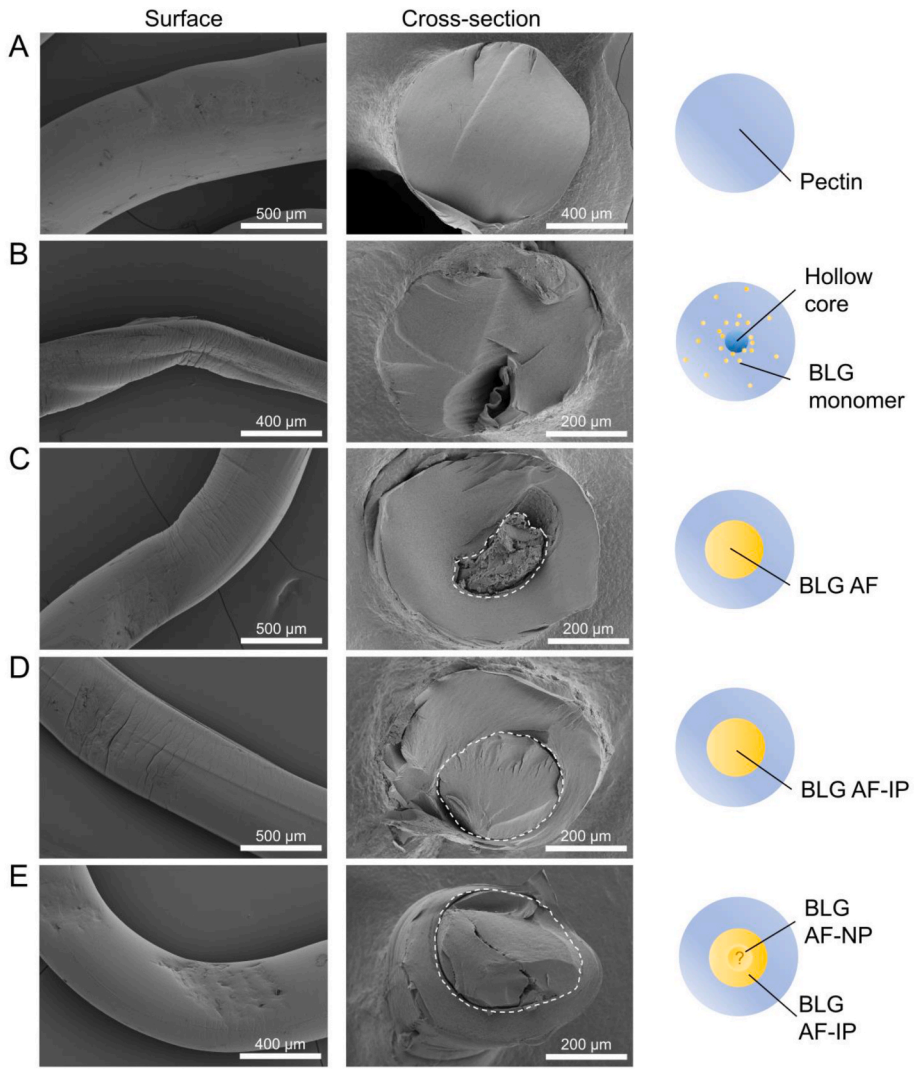

Fig. 2. SEM micrographs of the surface and cross-section of fibers prepared by chemical fixation and critical point drying to preserve their as-spun morphology. Fibers were spun from A: pectin; B: pectin-BLG monomer; C: pectin-BLG amyloid fibrils (AF); D: pectin-BLG isotropic phase amyloid fibrils (AF-IP); E: pectin-BLG isotropic/nematic phase amyloid fibrils (AF-IP/NP). The intended double core structure for fibers with BLG AF-NP inside BLG AF-IP in the last row was not distinguishable experimentally. The flow rate for pectin was 10 mL/h, for BLG monomer, AF, and AF-IP 2 mL/h, and for BLG AF-NP 0.1 mL/h. Schematics illustrate the theoretical cross-sectional morphology. The scale bars represent 500, 400, and 200 μm, respectively.

NP) (Fig. 2 C – E). The intended double core structure for fibers with BLG AF-NP inside BLG AF-IP was, however, not clearly distinguishable, presumably as a consequence of the minimal composition difference of the nematic and isotropic phases. The core section took up 14% (BLG AF), 34% (BLG AF-IP), and 56% (BLG AF-IP/NP) of the overall cross-sectional area of the fibers, respectively. Compared to the protein content of the fibers (Table 1), there seemed to be a link between a larger core diameter and a higher protein content of the fibers.

Fiber diameters measured from the cross-section micrographs were in the range of the diameters measured for the fibers in the wet state of 478–855 μm (Table 1). No clear correlations were found between the flow rates, the core material, and the fiber diameters in the wet state. A possible reason is that the diameter of the fibers was mainly determined by the fixed diameter of the glass capillary outlet. After drying, the diameter of the fibers shrank by 72–86% to 107–135 μm. Again, no clear correlation between the spinning parameters and the diameters was observed. Comparing the diameters of the dry fibers with their dry matter, however, showed that the fibers with the highest dry matter also had the largest diameters in the dry state (Table 1).

3.4. Orientation and degree of alignment

3.4.1. Scattering patterns

Since the bulk properties of materials are related to their internal structure (Morozova et al., 2021), synchrotron wide-angle X-ray scattering (WAXS) experiments were performed to gain insights into the structure, composition, and the alignment of the individual components of the pectin-BLG fibers. The influences of the flow rates during spinning and the different conformational states of BLG in the core were studied. The cross-sections of dried fibers (diameters ~120 μm) were measured vertically with a step size of 20 μm with a 17 μm X-ray beam (Fig. 3 A i). The spatial resolution allowed different portions of the cross-section to be measured. Scattering patterns were generated of just the pectin shell (at the outer layer), as well as of the pectin shell and the BLG core (at the center of the fibers).

The 2D scattering patterns (Fig. 3 A ii) at the center have the most information about the core-shell structure, since they are composed of all the phases. These 2D patterns were integrated as the scattering intensity (I) as a function of the scattering vector (q) (Fig. 3 A iii) for all fibers (Fig. 3 B). This relationship of phases generally depends on the spatial distribution of polymer strands within the material (Morozova et al., 2021).

The scattering curves have three main peaks: P1, P2, and P3. P1 at $q = 8\ nm^{-1}$ corresponds to a real-space distance d of 0.785 nm. The diffuse scattering over a broader q-range at this position represents amorphous structures in horizontal orientation parallel to the fiber axis (Salditt et al., 1994). P1 was found for all samples at every scanning position including the ones of only the pectin shell of the fibers (for a complete overview of scattering patterns see Supplementary Data Fig. S5). Since polymer clustering or gelation can give rise to diffuse-like scattering, it was concluded that this peak represents the vertical distance between the polymer chains of the Ca^{2+}-induced pectin gel. According to the

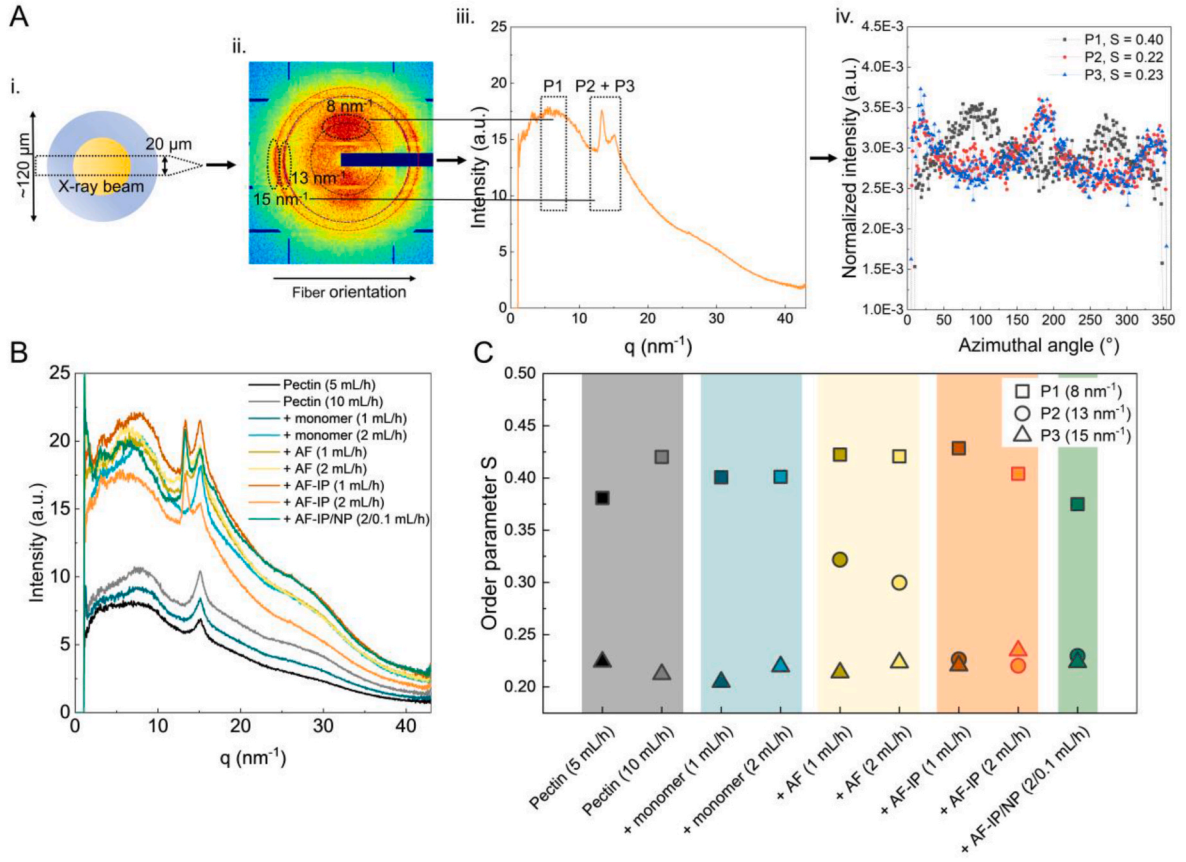

Fig. 3. A: WAXS analysis of the molecular alignment in the fibers exemplarily shown for pectin-BLG AF-IP (2 mL/h) fibers. i. Fibers of about 120 µm diameter were scanned in 20 µm steps perpendicular to their axis with an X-ray beam of 17 µm. For each fiber, the scattering pattern that contained contributions from both components (pectin and BLG) was selected. ii. 2D scattering pattern at the center of the fiber. iii. Scattering intensity (I) as a function of scattering vector (q), showing the contribution of both components (pectin and BLG AF-IP). iv. Scattering intensity (I) as a function of azimuthal angle (χ) for the center of pectin-BLG AF-IP (2 mL/h); B: influence of fiber composition on azimuthally integrated (I vs q) WAXS patterns, measured at the center of dried fibers. The q-values P1 = 8 nm^{-1}, P2 = 13 nm^{-1}, and P3 = 15 nm^{-1} were used to calculate the order parameter (S); C: order parameter (S) at P1 – 3 calculated from the radially integrated (I vs χ) WAXS patterns as a function of fiber composition and flow rate. The representative sample from A (pectin-BLG AF-IP (2 mL/h)) is highlighted in red.

adjusted "egg-box", the gelation takes place as a two-stage process where initially pectin dimers associate strongly before weaker inter-dimer associations are formed (Braccini & Pérez, 2001). SAXS measurements of pectins undergoing a Ca^{2+}-induced sol-gel transition have indicated junction zones that can be viewed as rod-like cylinders whose cross-sectional radius increased from 0.3 to 0.8 nm with an increased amount of added Ca^{2+} (Axelos et al., 1991). Further SAXS investigations have shown that the cross-sectional radius of gyration (R_c) of the pectin junction zones increases with a lower degree of esterification. R_c values of 0.63 and 0.85 nm were measured for pectins with DE values of 71% and 63%, respectively (Schuster et al., 2011). The reported cross-sectional radii agree with the determined vertical distance of 0.785 nm in the present study.

The clear scattering peaks at 13 and 15 nm^{-1} indicate the presence of crystalline structures. P2 at q = 13 nm^{-1} corresponds to d = 0.483 nm. This peak was only observable for samples containing BLG amyloid fibrils in their core. It was suggested that P2 represents the repetitive horizontal distance between amyloid β-strands which run perpendicular to the axis of the amyloid fibril itself, as well as to the axis of the pectin-BLG fiber. This is in line with typical X-ray diffraction patterns of amyloid fibrils with a reflection at 0.47–0.48 nm corresponding to the inter-strand distance of their cross-β structure (Dharmadana et al., 2017; Wei et al., 2017).

At P3 with q = 15 nm^{-1}, d is 0.419 nm which may correspond to the pitch of the pectin helices perpendicular to the fiber axis. Our understanding of the conformation of pectin in realistic systems that consider side chains, functional groups, and complexes is still limited. However, a simplified pectin backbone made of homogalacturonan with three monomers per one helix turn has been shown to have a pitch of 0.43 nm per monomer, (Pérez et al., 2000). The same pitch was determined by X-ray diffraction analysis for Ca^{2+}-induced pectin gel (Walkinshaw & Arnott, 1981). Furthermore, NMR measurements resulted in values of 0.4–0.45 nm (Catoire et al., 1997). Those reported values agree well with the determined value of 0.419 nm.

3.4.2. Order parameter

Alignment of the structures at P1 – 3 was expressed as the order parameters (S) and calculated based on the radially integrated scattering intensities at P1 – 3 as a function of the azimuthal angle (Fig. 3 C). Full alignment is represented by an S of 1, whereas random orientation equals 0. This analysis process is exemplarily depicted in Fig. 3 A for the pectin fiber containing BLG AF-IP (2 mL/h). Here, the scattering intensity from the 2D pattern (Fig. 3 A ii) was integrated azimuthally around the rings related to peaks P1 – P3, as the scattering intensity (I) as a function of the azimuthal angle (χ) (Fig. 3 A iv). Since all order parameters were determined from dried fiber samples that also experienced shrinkage, it was assumed that the overall molecular alignment might be higher in the hydrated fibers.

For pure pectin fibers, S_{P1}, representing the alignment of pectin chains parallel to the fiber axis, increased from 0.38 to 0.42 with increasing the flow rate from 5 to 10 mL/h. This has already been observed for fibers of pure alginate (Hu et al., 2018) and alginate with BLG nanofibrils (Kamada et al., 2020), both gelled with calcium ions, where higher flow rates resulted in a higher structural alignment in the

fibers.

All core-shell fibers were spun with a pectin flow rate of 10 mL/h, yet all samples had an S_{P1} at the core with equal or lower values than pure pectin fibers, meaning less alignment. This is most likely due to the overlapping scattering of the pectin shell and the BLG core at the fiber center, which cannot be separated.

For samples spun with BLG monomer, S_{P1} stayed constant at 0.40 with a core flow rate increase from 1 to 2 mL/h. This stability led to the conclusion that the incorporation of the small (~18 kDa) and globular BLG monomers (Kinsella & Whitehead, 1989) had little influence on the shear-induced alignment of the pectin molecules. The microstructure (Fig. 2 B) and the low protein content of the pectin-BLG monomer fibers (Table 1) strengthened this conclusion.

For fibers spun with BLG AF, changing the core flow rate from 1 to 2 mL/h did not alter S_{P1}. For BLG AF-IP as the core material, S_{P1} decreased from 0.43 to 0.40 with an increased core flow rate. When using a higher core flow rate, the protein content in these fibers only increased by 2.4% for BLG AF, but by 7.4% for BLG AF-IP (Table 1). This larger increase in protein content might have disturbed the pectin alignment or increased the contribution of the BLG core to the scattering of the pectin shell, ultimately decreasing S_{P1}. The lowest S_{P1} was found for fibers with a BLG AF-IP/NP double core (0.37). The even more complex composition of the protein core might have interfered with pectin alignment or the scattering signal of the pectin shell. Since the protein content of these fibers could not be determined, the increased protein core diameter for these samples (see Chapter 3.3) provided evidence that the larger protein core led to the decrease of S_{P1}. These results mean that the pectin shell which is exposed to high shear at the wall has high alignment, while the organization of the core remains rather random.

The order parameter, S_{P2}, reflecting the repetitive horizontal distance between amyloid β-strands perpendicular to the fiber axis, decreased from 0.32 to 0.30 for BLG AF when increasing the core flow rate from 1 to 2 mL/h. For BLG AF-IP, it stayed lower at ~0.22. Based on the previously discussed observation of rope coiling (see Chapter 3.1), it was concluded that the increased ratio of the flow rates Q_{inner}/Q_{outer} enhanced this effect and ultimately reduced the alignment of fibrillar proteins parallel to the fiber axis.

S_{P3} as a measure of aligned pectin helices perpendicular to the fiber axis ranged between 0.20 and 0.23 for all fiber samples. It was concluded that neither the flow rate nor the introduction of a BLG core to the fibers influenced the orientation of the pectin helices perpendicular to the fiber axis in a meaningful way.

3.5. Mechanical properties

In order to understand how the conformation of BLG in the fiber core, the spinning flow rates, and the subsequent molecular alignment affect the mechanical properties of the fibers, tensile testing of the dried fibers was performed. Young's modulus, ultimate tensile strength, and elongation at break were calculated from the recorded stress-strain curves (Fig. 4, for representative stress-strain curves see Supplementary Data Fig. S6).

3.5.1. Pectin

Fibers produced from pure pectin at 5 mL/h showed Young's modulus, ultimate tensile strength, and elongation at break of 1.7 GPa, 59.2 MPa, and 8.3%. Young's modulus and ultimate tensile strength increased to 3.0 GPa and 117.0 MPa with increasing the pectin flow rate to 10 mL/h – analogous to the increase of the order parameter S_{P1} (Fig. 3 C), representing the alignment of pectin chains parallel to the fiber axis. Elongation at break was not influenced statistically significantly. In studies on fibers of cellulose (Iwamoto et al., 2011), pure alginate (Hu et al., 2018) and alginate with BLG nanofibrils (Kamada et al., 2020), both gelled with calcium ions, the increased shear-induced alignment and molecular orientation at higher flow rates resulted in increased stiffness (i.e., Young's modulus) and higher strength (i.e., ultimate tensile strength).

3.5.2. Pectin-BLG monomers (mono)

Compared to pure pectin fibers spun at 10 mL/h, the addition of BLG monomer at a flow rate of 1 mL/h as the core material did not significantly change Young's modulus and ultimate tensile strength. These parameters only changed from 3.0 GPa to 117.0 MPa for pure pectin to 2.4 GPa and 80.0 MPa for pectin-BLG monomer. At a flow rate combination of 10 mL/h for pectin and 2 mL/h for BLG monomer, Young's modulus (7.0 GPa) and ultimate tensile strength (201.4 GPa) were significantly larger than for pure pectin fibers spun at a flow rate of 10 mL/h, despite the order parameter S_{P1} being lower (Fig. 3 C). The absence of a clear core-shell structure in these fibers (Fig. 2 B) led to the conclusion that small amounts of positively charged BLG monomer molecules randomly dispersed within the Ca^{2+}-gelled pectin network may act as antiplasticizers by reducing electrostatic repulsion between negatively charged pectin molecules, resulting in better inter-chain alignment and the promoted formation of "egg-box" bundles (John et al., 2019). Such antiplasticization effects at low concentrations of small molecules that have strong interactions with the matrix they are embedded in have been previously described for food-relevant systems (Chang et al., 2006; Seow, 2010; Ubbink, 2016). This effect might have resulted in the increased mechanical properties of the pectin-BLG monomer fibers.

3.5.3. Pectin-BLG amyloid fibrils (AF) and BLG isotropic phase amyloid fibrils (AF-IP)

When BLG AF were used as the core material at a flow rate of 1 mL/h,

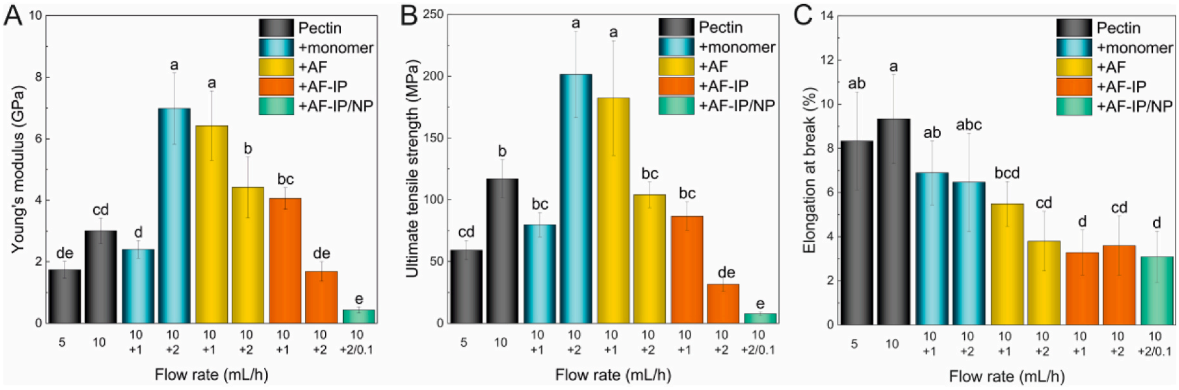

Fig. 4. Effect of composition and spinning flow rates on the mechanical properties of dried fibers consisting of pectin and pectin-BLG monomer/amyloid fibrils (AF)/isotropic phase amyloid fibrils (AF-IP)/isotropic phase amyloid fibrils and nematic phase amyloid fibrils (AF-IP/NP). A: Young's modulus; B: ultimate tensile strength; C: elongation at break. Flow rates for pectin were 5 or 10 mL/h. Flow rates for BLG monomer/AF/AF-IP were 1 (+1) or 2 (+2) mL/h and for AF-NP 0.1 (+0.1) mL/h. Lowercase letters (a, b, c, d, e) indicate statistically significant differences between the samples ($p < 0.05$).

Young's modulus and ultimate tensile strength were similar to the fibers spun with BLG monomer at a flow rate of 2 mL/h. However, increasing the BLG AF flow rate to 2 mL/h led to a decrease of these parameters. The same trend was observed with BLG AF-IP as core material, although for BLG AF-IP the absolute values for Young's modulus and ultimate tensile strength were lower than for BLG AF.

Nanomechanical testing on individual amyloid fibrils showed that they tend to be brittle and stiff with Young's moduli in the GPa range, which is remarkably high compared to other biological materials (Knowles & Buehler, 2011; Paparcone & Buehler, 2011; Solar & Buehler, 2013). This stiffness originates largely from the dense intermolecular hydrogen bonds between β-sheet structures in the aligned backbones of fibrils (Adamcik et al., 2010). This also explains why elongation at break was lower for all samples containing BLG AF compared to fibers containing no BLG or BLG in its monomeric form (Fig. 4 C). Elongation at break reflects the capability of a sample to deform elastically and plastically before fracturing. BLG in its brittle amyloid conformation decreases the ductility of the fibers. Kamada et al. (2020) also discovered that fibers spun from blends of alginate with BLG monomers were more ductile than fibers made from blends with BLG amyloid fibrils.

However, combining individual amyloid fibrils into bundles can decrease their stiffness (i.e., Young's modulus). Fibrils sliding past each other under deformation allows them to deform more elastically (Solar & Buehler, 2013). At higher core flow rates, pectin-BLG AF and -BLG AF-IP fibers had higher protein contents (Table 1), hence presumed thicker protein cores with more leeway for the individual amyloid fibrils to slide past each other without breakage under strain.

The decreased ultimate tensile strength at higher core flow rates for fibers made with BLG AF and AF-IP was in line with the decrease of the order parameter S_{P2} (representing the amyloid β-strands running perpendicular to the fiber axis) upon applying a higher core flow rate (Fig. 3 C). Together with the previously discussed observation of rope coiling (see Chapter 3.1), it was concluded that the increased ratio of the flow rates Q_{inner}/Q_{outer} enhanced the helical bending of the BLG core and ultimately reduced the alignment of fibrillar proteins parallel to the fiber axis.

Furthermore, the BLG AF-IP had a contour length of 0.2 ± 0.1 μm as determined by AFM analysis (see Supplementary Data Fig. S7) whereas the non-shortened BLG AF were several micrometers long. In the study by Kamada et al. (2017) microfibers were made from either short curved or long straight BLG amyloid fibrils gelled by acetate buffer (pH 5.2). Short, curved fibrils led to fibers with higher mechanical strength despite the degree of fibril alignment being lower compared to fibers made with long and straight fibrils. The authors conclude that the underlying mechanism for the fiber stabilization is the interlocking of the curved amyloid fibrils due to molecular entanglement. As opposed to the findings of Kamada et al. (2017), a study by Ye et al. (2022) compared the mechanical properties of microfibers also assembled from long straight and short curved BLG amyloid fibrils but cross-linked by genipin. In this case, the fibers made from straight amyloid fibrils had a higher Young's modulus, higher stress at break, and higher elongation at break compared to the fibers made from the shorter curved amyloid fibrils. It is suggested that the higher modulus originates from the higher modulus of individual straight amyloid fibrils, indicated by their higher persistence length. Furthermore, the straight amyloid fibrils exhibited a higher degree of alignment. We conclude that for spinning procedures such as the one of Ye et al. (2022) and the presented pectin core-shell fibers where the stability of the microfibers does not primarily depend on the entanglement of the PNF building blocks, a higher degree of molecular alignment parallel to the fiber axis is preferable in terms of mechanical properties.

3.5.4. Pectin-BLG isotropic and nematic phase amyloid fibrils (AF-IP/NP)

The weakest fibers in terms of measured mechanical properties were the core-shell fibers made from pectin with a double core of BLG AF-IP/NP. Their Young's modulus was 0.4 GPa and their ultimate tensile strength was 7.9 MPa. In this case, the core material consisted of rather short (AF-IP: 224 ± 113 nm; AF-NP: 415 ± 212 nm) BLG amyloid fibrils. Furthermore, low alignment of the amyloid fibrils parallel to the fiber axis was assumed because of the observed low value for the order parameter S_{P2} (Fig. 3 C) – presumably a result of rope coiling of the BLG-core jet. Under these conditions, neither molecular entanglement nor directional alignment could effectively contribute to the mechanical stability of the spun fiber.

3.5.5. Comparison to other microfibers with amyloid fibrils

The mechanical properties of the pectin-BLG fibers were compared to the ones from previous studies on structuring amyloid fibrils into hierarchically ordered fibers using different approaches. Spinning of hen egg white lysozyme amyloid fibers with gellan gum based on interfacial polyion complexation led to fibers with Young's moduli of 6.8–10.4 GPa, ultimate tensile stress of 201–265 MPa, and ultimate elongation of 3.2–8.7% (Meier & Welland, 2011). This was comparable to the pectin-BLG AF core-shell fibers with 6.4–7.0 GPa, 104–182 MPa, and 3.8–5.5%, respectively. BLG amyloid fibers blended with alginate and gelled with $CaCl_2$ with Young's modulus of 1.7–2.5 GPa, ultimate tensile stress of ~45–55 MPa, and the ultimate elongation of 8–15% were weaker, yet more elastic and ductile (Kamada et al., 2020). Fibers made from either curved or straight BLG amyloid fibrils gelled with acetate buffer (pH 5.2) and cross-linked with genipin displayed Young's moduli, ultimate tensile stress, and elongation at break of 0.4 and 1.6 GPa, 6.1 and 20.4 MPa, and 10.4 and 2%, respectively (Ye et al., 2022). In comparison, the core-shell pectin-BLG AF fibers are stiffer, stronger, and minimally more ductile.

Overall, the results demonstrate that the incorporation of a BLG core to pectin fibers can enhance their mechanical properties, i.e., a higher stiffness in the linear elastic region and higher ultimate tensile strength. This was observed for BLG in monomeric conformation as well as for amyloid fibrils if the appropriate flow rates were chosen during microfluidic spinning. Thus, flow rates should account for the interplay of different protein conformations and molecular alignment in the fibers during spinning.

3.6. BLG core-shell fibers with alginate

When it comes to wet and microfluidic spinning of hydrogels, one of the most frequently used hydrocolloids is alginate (Chen, Jones, & Campanella, 2021; Hu et al., 2018; Pendyala et al., 2019; Sun et al., 2018). It is nontoxic and biocompatible (Uyen et al., 2020) and easily gels with Ca^{2+} ions under mild conditions similar to pectin. In the last step of the study, the coaxial microfluidic spinning setup (Fig. 5 A) was used to produce microfibers from BLG amyloid fibrils with an alginate shell instead of a pectin shell.

During spinning, a clear interface between the inner BLG AF jet and the outer alginate solution was observed using polarized light microscopy (Fig. 5 A). Again, SEM was used to study the cross-section morphology of the dried fibers. Pure alginate fibers had a uniform cross-section just like pure pectin fibers whereas alginate-BLG AF fibers had a clear core-shell structure (Fig. 5 B).

CLSM imaging of the wet as-spun alginate fibers with their amyloid fibril core stained with thioflavin T (Fig. 5 C, visualized in yellow) allowed deeper insights into their core-shell structure. Since alginate was not stained and does not exhibit autofluorescence, the reflection mode of the CLSM was used to visualize the contour of the alginate shell (Fig. 5 C, visualized in blue). Just like during spinning, the boundary between the BLG AF core and the alginate shell was sharp and clearly observable in the final fiber, which suggests little mass transfer between the inner and outer jets during spinning. The previously discussed rope coiling of the BLG AF core jet in pectin-BLG fibers (see Chapter 3.1) was confirmed by the images of alginate-BLG AF fibers. The protein core is again not straight and concentric but shows helical bending. These experiments demonstrated that the concept of microfluidically spun core-

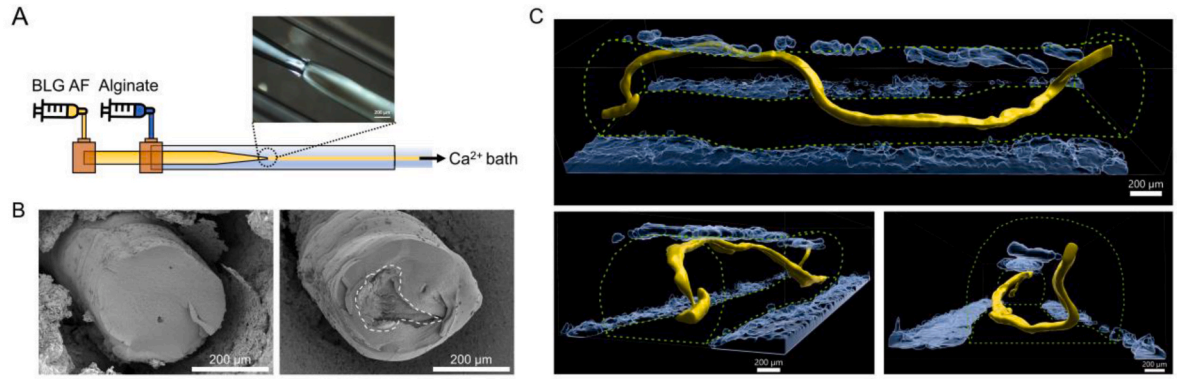

Fig. 5. Production and characterization of alginate-BLG amyloid fibril (AF) fibers by coaxial microfluidic spinning. A: schematic illustration of the capillary microfluidic setup used to produce fibers. The polarized light optical micrograph shows the generation of a birefringent cylindrical core jet in the capillary during spinning; B: SEM micrographs of the cross-sections of fibers prepared by chemical fixation and critical point drying to preserve their as-spun morphology; left: alginate; right: alginate-BLG AF; C: 3D reconstruction of CLSM micrographs of as-spun alginate-BLG AF fibers. The BLG AF core is stained with thioflavin T and displayed in yellow. Blue areas indicate the topography of the fiber surface as recorded by CLSM in reflection mode. Dashed green lines indicate the overall outline of the fiber. The scale bars represent 200 μm.

shell hydrocolloid fibers with BLG amyloid fibrils as the core material is general enough to be applied to multiple polysaccharides, and benchmarked to both pectin and alginate as the shell material. For future experiments, these observations will allow fine-tuning of flow rates, spinning solution viscosities, and capillary dimensions to achieve the desired fiber core morphology (i.e., straight or twisted) associated with the corresponding mechanical properties.

4. Conclusions

The successful fabrication of hierarchically assembled core-shell fibers from pectin and BLG was achieved by coaxial microfluidic spinning and gelation with $CaCl_2$. This process does not require either toxic or costly chemical cross-linking agents. Especially in food science where edible proteinaceous fibers for meat analogs with reasonable mechanical strength are highly sought after, the here presented spinning approach could take on greater significance.

The pectin shell provides mechanical strength to the fibers that is significantly affected by the conformation of BLG in the core and can be tuned by adapting the flow rate of the core jet. BLG in its monomeric conformation does not result in fibers with a spatially divided protein core and a polysaccharide shell, but instead diffuses into and through the outer pectin matrix. This leads to fibers with low protein content, but enhanced strength compared to pure pectin fibers likely because of ionic interactions of the protein and the polysaccharide. Using BLG amyloid fibrils led to fibers with clear core-shell structures and increased molecular alignment of the protein core. These fibers had higher Young's moduli and ultimate tensile strength compared to pure pectin fibers. Full length BLG amyloid fibrils proved to be more beneficial to the mechanical properties than shortened amyloid fibrils. Nonetheless, increasing the core flow rate beyond an optimum value resulted in bending instabilities and rope coiling of the protein core. The lower molecular alignment along the fiber axis then proved disadvantageous for the mechanical performance.

In conclusion, the presented insights into the relationship between protein conformation, spinning flow rate, and resulting mechanical properties of core-shell microfibers are fundamentally and practically important for shaping and enhancing mechanical properties of novel fibrous proteinaceous materials by addressing their molecular alignment.

The presented gentle and food-grade spinning process is not limited to pectin and BLG, but has a general significance as demonstrated by the successful fabrication of alginate-BLG fibers. The substitution of BLG with plant-based proteins able to form amyloid fibrils is likely realizable. Thus, these findings suggest the potential of producing and improving multiphasic fiber systems using natural proteins and hydrocolloids to create new biomaterials with various mechanical and functional properties in fields such as bioengineering and food science.

Funding

This research project was supported by grants from Motif FoodWorks, Inc.

Author contributions

Ines Kutzli: Conceptualization, investigation, formal analysis, visualization, writing – original draft. **Viviane Lutz-Bueno:** WAXS investigation, analysis, writing – review & editing. **Massimo Bagnani:** investigation, formal analysis, visualization, writing – review & editing. **Ana Diaz:** WAXS measurements, writing – review & editing. **Hamed Almohammadi:** Methodology, writing – review & editing. **Reed A. Nicholson:** Project administration, supervision, writing – review & editing. **Stefan K. Baier:** Project administration, supervision, writing – review & editing. **Raffaele Mezzenga:** Project conceptualization and design, administration, supervision, funding acquisition, writing – review & editing.

Declaration of competing interest

The authors have no conflict of interest to declare.

The views expressed in this article are those of the authors and do not necessarily reflect the position or policy of Motif FoodWorks, Inc.

Data availability

Data will be made available on request.

Acknowledgments

The authors thank Stephan Handschin and Dr. Tobias Schwarz of ScopeM for their support & assistance in this work. Furthermore, the authors would like to thank Herbstreith & Fox GmbH & Co. KG (Neuenbürg, Germany) for generously providing pectin samples. We acknowledge the beamtime for scanning-WAXS measurements at the cSAXS beamline of the SLS, PSI, under proposal 20210413.

Appendix A. Supplementary data

Supplementary data to this article can be found online at https://doi.org/10.1016/j.foodhyd.2023.108845.

References

Adamcik, J., Jung, J. M., Flakowski, J., De Los Rios, P., Dietler, G., & Mezzenga, R. (2010). Understanding amyloid aggregation by statistical analysis of atomic force microscopy images. *Nature Nanotechnology, 5*(6), 423–428. https://doi.org/10.1038/nnano.2010.59

Almohammadi, H., Bagnani, M., & Mezzenga, R. (2020). Flow-induced order-order transitions in amyloid fibril liquid crystalline tactoids. *Nature Communications, 11*, 5416. https://doi.org/10.1038/s41467-020-19213-x

Axelos, M. A. V., Garnier, C., & Thibault, J.-F. (1991). An example of ionic complexation in biopolymers: The pectin-calcium system. *AIP Conference Proceedings, 226*, 569–580. https://doi.org/10.1063/1.40576

Bolisetty, S., Adamcik, J., & Mezzenga, R. (2011). Snapshots of fibrillation and aggregation kinetics in multistranded amyloid β-lactoglobulin fibrils. *Soft Matter, 7*(2), 493–499. https://doi.org/10.1039/c0sm00502a

Braccini, I., & Pérez, S. (2001). Molecular basis of Ca^{2+}-induced gelation in alginates and pectins: The egg-box model revisited. *Biomacromolecules, 2*(4), 1089–1096. https://doi.org/10.1021/bm010008g

Burgess, K. J., & Downey, G. (1979). Effect of coagulation bath composition on the composition and texture of casein-carrageenan fibres. *Irish Journal of Food Science & Technology, 3*(2), 151–157. http://www.jstor.org/stable/25557985.

Cao, Y., Bolisetty, S., Adamcik, J., & Mezzenga, R. (2018). Elasticity in physically cross-linked amyloid fibril networks. *Physical Review Letters, 120*(15), Article 158103. https://doi.org/10.1103/PhysRevLett.120.158103

Cao, L., Lu, W., Mata, A., Nishinari, K., & Fang, Y. (2020). Egg-box model-based gelation of alginate and pectin: A review. *Carbohydrate Polymers, 242*, Article 116389. https://doi.org/10.1016/j.carbpol.2020.116389

Cao, Y., & Mezzenga, R. (2019). Food protein amyloid fibrils: Origin, structure, formation, characterization, applications and health implications. *Advances in Colloid and Interface Science, 269*, 334–356.

Catoire, L., Derouet, C., Redon, A. M., Goldberg, R., & Hervé Du Penhoat, C. (1997). An NMR study of the dynamic single-stranded conformation of sodium pectate. *Carbohydrate Research, 300*, 19–29. https://doi.org/10.1016/S0008-6215(97)00035-9

Chang, Y. P., Abd Karim, A., & Seow, C. C. (2006). Interactive plasticizing-antiplasticizing effects of water and glycerol on the tensile properties of tapioca starch films. *Food Hydrocolloids, 20*(1), 1–8. https://doi.org/10.1016/j.foodhyd.2005.02.004

Chen, D., Jones, O. G., & Campanella, O. H. (2021). Plant protein-based fibers: Fabrication, characterization, and potential food applications. *Critical Reviews in Food Science and Nutrition*. https://doi.org/10.1080/10408398.2021.2004991

Chen, Z., Song, J., Xia, Y., Jiang, Y., Murillo, L. L., Tsigkou, O., Wang, T., & Li, Y. (2021). High strength and strain alginate fibers by a novel wheel spinning technique for knitting stretchable and biocompatible wound-care materials. *Materials Science and Engineering: C, 127*, Article 112204. https://doi.org/10.1016/j.msec.2021.112204

Cui, B., Liang, H., Li, J., Zhou, B., Chen, W., Liu, J., & Li, B. (2022). Development and characterization of edible plant-based fibers using a wet-spinning technique. *Food Hydrocolloids, 133*, Article 107965. https://doi.org/10.1016/j.foodhyd.2022.107965

Dharmadana, D., Reynolds, N. P., Conn, C. E., & Valéry, C. (2017). Molecular interactions of amyloid nanofibrils with biological aggregation modifiers: Implications for cytotoxicity mechanisms and biomaterial design. *Interface Focus, 7*(4), Article 20160160. https://doi.org/10.1098/rsfs.2016.0160

Downey, G., & Burgess, K. J. (1979). Texture studies on edible protein fibres produced by a wet spinning technique I. Fibres produced from casein and carrageenan. *International Journal of Food Science and Technology, 14*(1), 33–40. https://doi.org/10.1111/j.1365-2621.1979.tb00844.x

Du, X. Y., Li, Q., Wu, G., & Chen, S. (2019). Multifunctional micro/nanoscale fibers based on microfluidic spinning technology. *Advanced Materials, 31*(52), Article 1903733. https://doi.org/10.1002/adma.201903733

Fletcher, D. L., & Ahmed, E. M. (1977). Spinning of peanut protein fibers. *Peanut Science, 4*(1), 17–21. https://doi.org/10.3146/i0095-3679-4-1-5

Gallant, D. J., Bouchet, B., Culioli, J., & Ultrastructural, J. C. (1984). Ultrastructural aspects of spun pea and fababean proteins. *Food Microstructure, 3*(2), 175–183. https://hal.inrae.fr/hal-02727621.

He, H., Sevick, E. M., & Williams, D. R. M. (2016). Isotropic and nematic liquid crystalline phases of adaptive rotaxanes. *Journal of Chemical Physics, 144*(12), Article 124901. https://doi.org/10.1063/1.4943098

Huang, H. C., Hammond, E. G., Reitmeier, C. A., & Myers, D. J. (1995). Properties of fibers produced from soy protein isolate by extrusion and wet-spinning. *Journal of the American Oil Chemists' Society, 72*(12), 1453–1460. https://doi.org/10.1007/BF02577837

Hu, X., Liu, S., Zhou, G., Huang, Y., Xie, Z., & Jing, X. (2014). Electrospinning of polymeric nanofibers for drug delivery applications. *Journal of Controlled Release, 185*, 12–21. https://doi.org/10.1016/j.jconrel.2014.04.018

Hu, X., Tian, M., Sun, B., Qu, L., Zhu, S., & Zhang, X. (2018). Hydrodynamic alignment and microfluidic spinning of strength-reinforced calcium alginate microfibers. *Materials Letters, 230*, 148–151. https://doi.org/10.1016/j.matlet.2018.07.092

Iwamoto, S., Isogai, A., & Iwata, T. (2011). Structure and mechanical properties of wet-spun fibers made from natural cellulose nanofibers. *Biomacromolecules, 12*(3), 831–836. https://doi.org/10.1021/bm101510r

Jiang, H., Hu, Y., Zhao, P., Li, Y., & Zhu, K. (2006). Modulation of protein release from biodegradable core-shell structured fibers prepared by coaxial electrospinning. *Journal of Biomedical Materials Research, Part B: Applied Biomaterials, 79B*, 50–57. https://doi.org/10.1002/jbm.b.30510

John, J., Ray, D., Aswal, V. K., Deshpande, A. P., & Varughese, S. (2019). Dissipation and strain-stiffening behavior of pectin-Ca gels under Laos. *Soft Matter, 15*(34), 6852–6866. https://doi.org/10.1039/c9sm00709a

Jun, Y., Kang, E., Chae, S., & Lee, S. H. (2014). Microfluidic spinning of micro- and nano-scale fibers for tissue engineering. *Lab on a Chip, 14*(13), 2145–2160. https://doi.org/10.1039/c3lc51414e

Kamada, A., Levin, A., Toprakcioglu, Z., Shen, Y., Lutz-Bueno, V., Baumann, K. N., Mohammadi, P., Linder, M. B., Mezzenga, R., & Knowles, T. P. J. (2020). Modulating the mechanical performance of macroscale fibers through shear-induced alignment and assembly of protein nanofibrils. *Small, 16*(9), Article 1904190. https://doi.org/10.1002/smll.201904190

Kamada, A., Mittal, N., Söderberg, L. D., Ingverud, T., Ohm, W., Roth, S. V., Lundell, F., & Lendel, C. (2017). Flow-Assisted assembly of nanostructured protein microfibers. *Proceedings of the National Academy of Sciences of the United States of America, 114*(6), 1232–1237. https://doi.org/10.1073/pnas.1617260114

Kinsella, J. E., & Whitehead, D. M. (1989). Proteins in whey: Chemical, physical, and functional properties. *Advances in Food & Nutrition Research, 33*, 343–438. https://doi.org/10.1016/S1043-4526(08)60130-8

Knowles, T. P. J., & Buehler, M. J. (2011). Nanomechanics of functional and pathological amyloid materials. *Nature Nanotechnology, 6*(8), 469–479. https://doi.org/10.1038/nnano.2011.102

Knowles, T. P. J., & Mezzenga, R. (2016). Amyloid fibrils as building blocks for natural and artificial functional materials. *Advanced Materials, 28*(31), 6546–6561. https://doi.org/10.1002/adma.201505961

Kumar, T. S. M., Senthil Kumar, K., Rajini, N., Siengchin, S., Ayrilmis, N., & Varada Rajulu, A. (2019). A comprehensive review of electrospun nanofibers: Food and packaging perspective. *Composites Part B: Engineering, 175*(June), Article 107074. https://doi.org/10.1016/j.compositesb.2019.107074

Kutzli, I., Gibis, M., Baier, S. K., & Weiss, J. (2019). Electrospinning of whey and soy protein mixed with maltodextrin – influence of protein type and ratio on the production and morphology of fibers. *Food Hydrocolloids, 93*, 206–214. https://doi.org/10.1016/j.foodhyd.2019.02.028

Liu, R., Kong, B., Chen, Y., Liu, X., & Mi, S. (2020). Formation of helical alginate microfibers using different G/M ratios of sodium alginate based on microfluidics. *Sensors and Actuators B: Chemical, 304*, Article 127069. https://doi.org/10.1016/j.snb.2019.127069

Li, T., Zhou, J., Peydayesh, M., Yao, Y., Bagnani, M., Kutzli, I., … Mezzenga, R. (2023). Plant protein amyloid fibrils for multifunctional sustainable materials. *Advanced Sustainable Systems, 7*(4), Article 2200414.

Liu, P., Xu, H., Zhao, Y., & Yang, Y. (2017). Rheological properties of soy protein isolate solution for fibers and films. *Food Hydrocolloids, 64*, 149–156. https://doi.org/10.1016/j.foodhyd.2016.11.001

Lutz-Bueno, V., Bolisetty, S., Azzari, P., Handschin, S., & Mezzenga, R. (2020). Self-winding gelatin–amyloid wires for soft actuators and sensors. *Advanced Materials, 32*(48), Article 2004941. https://doi.org/10.1002/adma.202004941

Meier, C., & Welland, M. E. (2011). Wet-spinning of amyloid protein nanofibers into multifunctional high-performance biofibers. *Biomacromolecules, 12*(10), 3453–3459. https://doi.org/10.1021/bm2005752

Moll, P., Salminen, H., Rausch, A., Schmitt, C., & Weiss, J. (2022). Adjusting the stickiness of concentrated pea protein – apple pectin systems via the biopolymer mixing ratio. *Future Foods, 6*, Article 100184. https://doi.org/10.1016/j.fufo.2022.100184

Morozova, S., Hitimana, E., Dhakal, S., Wilcox, K. G., & Estrin, D. (2021). Scattering methods for determining structure and dynamics of polymer gels. *Journal of Applied Physics, 129*, Article 071101. https://doi.org/10.1063/5.0033414

Mu, B., Xu, H., Li, W., Xu, L., & Yang, Y. (2019). Spinnability and rheological properties of globular soy protein solution. *Food Hydrocolloids, 90*, 443–451. https://doi.org/10.1016/j.foodhyd.2018.12.049

Nemati, S., Kim, S. J., Shin, Y. M., & Shin, H. (2019). Current progress in application of polymeric nanofibers to tissue engineering. *Nano Convergence, 6*, 36. https://doi.org/10.1186/s40580-019-0209-y

Nie, M., & Takeuchi, S. (2017). Microfluidics based synthesis of coiled hydrogel microfibers with flexible shape and dimension control. *Sensors and Actuators B: Chemical, 246*, 358–362. https://doi.org/10.1016/j.snb.2017.01.157

Nyström, G., Arcari, M., & Mezzenga, R. (2018). Confinement-induced liquid crystalline transitions in amyloid fibril cholesteric tactoids. *Nature Nanotechnology, 13*(4), 330–336. https://doi.org/10.1038/s41565-018-0071-9

Paparcone, R., & Buehler, M. J. (2011). Failure of Aβ(1-40) amyloid fibrils under tensile loading. *Biomaterials, 32*(13), 3367–3374. https://doi.org/10.1016/j.biomaterials.2010.11.066

Pendyala, G., Bithi, S. S., Vanapalli, S. A., & Fernandes, G. E. (2019). Continuous and high throughput production of alginate fibers using co-flow in a millifluidic T-junction. *Journal of Applied Polymer Science, 136*(9), Article 47120. https://doi.org/10.1002/app.47120

Pérez, S., Mazeau, K., & Hervé du Penhoat, C. (2000). The three-dimensional structures of the pectic polysaccharides. *Plant Physiology and Biochemistry, 38*(1/2), 37–55. https://doi.org/10.1016/S0981-9428(00)00169-8

Peydayesh, M., Bagnani, M., & Mezzenga, R. (2021). Sustainable bioplastics from amyloid fibril-biodegradable polymer blends. *ACS Sustainable Chemistry & Engineering, 9*(35), 11916–11926. https://doi.org/10.1021/acssuschemeng.1c03937

Peydayesh, M., Suter, M. K., Bolisetty, S., Boulos, S., Handschin, S., Nyström, L., & Mezzenga, R. (2020). Amyloid fibrils aerogel for sustainable removal of organic contaminants from water. *Advanced Materials, 32*(12), Article 1907932. https://doi.org/10.1002/adma.201907932

Ribe, N. M., Habibi, M., & Bonn, D. (2012). Liquid rope coiling. *Annual Review of Fluid Mechanics, 44*, 249–266. https://doi.org/10.1146/annurev-fluid-120710-101244

Salditt, T., Metzger, T. H., Peisl, J., & Jiang, X. (1994). Diffuse X-ray scattering of amorphous multilayers. *Journal de Physique III, 4*(9), 1573–1580. https://doi.org/10.1051/jp3:1994224

Schneider, C. A., Rasband, W. S., & Eliceiri, K. W. (2012). NIH image to ImageJ: 25 years of image analysis. *Nature Methods, 9*(7), 671–675. https://doi.org/10.1038/nmeth.2089

Schuster, E., Cucheval, A., Lundin, L., & Williams, M. A. K. (2011). Using SAXS to reveal the degree of bundling in the polysaccharide junction zones of microrheologically distinct pectin gels. *Biomacromolecules, 12*(7), 2583–2590. https://doi.org/10.1021/bm200578d

Seow, C. C. (2010). Antiplasticization of food polymer systems by low molecular mass diluents. In D. S. Reid, T. Sajjaanantakul, P. J. Lillford, & S. Charoenrein (Eds.), *Water properties in food, health, pharmaceutical and biological systems: ISOPOW* (Vol. 10, pp. 115–137). Wiley-Blackwell. https://doi.org/10.1002/9780470958193.ch8.

Shang, L., Yu, Y., Liu, Y., Chen, Z., Kong, T., & Zhao, Y. (2019). Spinning and applications of bioinspired fiber systems. *ACS Nano, 13*(3), 2749–2772. https://doi.org/10.1021/acsnano.8b09651

Sharifi, F., Sooriyarachchi, A. C., Altural, H., Montazami, R., Rylander, M. N., & Hashemi, N. (2016). Fiber based approaches as medicine delivery systems. *ACS Biomaterials Science & Engineering, 2*(9), 1411–1431. https://doi.org/10.1021/acsbiomaterials.6b00281

Singh, B., Kim, K., & Park, M. H. (2021). On-demand drug delivery systems using nanofibers. *Nanomaterials, 11*, 3411. https://doi.org/10.3390/nano11123411

Solar, M., & Buehler, M. J. (2013). Deformation behavior and mechanical properties of amyloid protein nanowires. *Journal of the Mechanical Behavior of Biomedical Materials, 19*, 43–49. https://doi.org/10.1016/j.jmbbm.2012.10.007

Sun, J., Chen, J., Liu, K., & Zeng, H. (2021). Mechanically strong proteinaceous fibers: Engineered fabrication by microfluidics. *Engineering, 7*(5), 615–623. https://doi.org/10.1016/j.eng.2021.02.005

Sun, T., Li, X., Shi, Q., Wang, H., Huang, Q., & Fukuda, T. (2018). Microfluidic spun alginate hydrogel microfibers and their application in tissue engineering. *Gels, 4*(2), 38. https://doi.org/10.3390/gels4020038

Tottori, S., & Takeuchi, S. (2015). Formation of liquid rope coils in a coaxial microfluidic device. *RSC Advances, 5*(42), 33691–33695. https://doi.org/10.1039/c5ra01037c

Ubbink, J. (2016). Structural and thermodynamic aspects of plasticization and antiplasticization in glassy encapsulation and biostabilization matrices. *Advanced Drug Delivery Reviews, 100*, 10–26. https://doi.org/10.1016/j.addr.2015.12.019

Usov, I., & Mezzenga, R. (2015). FiberApp: An open-source software for tracking and analyzing polymers, filaments, biomacromolecules, and fibrous objects. *Macromolecules, 48*(5), 1269–1280. https://doi.org/10.1021/ma502264c

Usuelli, M., Germerdonk, T., Cao, Y., Peydayesh, M., Bagnani, M., Handschin, S., Nyström, G., & Mezzenga, R. (2021). Polysaccharide-reinforced amyloid fibril hydrogels and aerogels. *Nanoscale, 13*(29), 12534–12545. https://doi.org/10.1039/d1nr03133c

Uyen, N. T. T., Hamid, Z. A. A., Tram, N. X. T., & Ahmad, N. (2020). Fabrication of alginate microspheres for drug delivery: A review. *International Journal of Biological Macromolecules, 153*, 1035–1046. https://doi.org/10.1016/j.ijbiomac.2019.10.233

Vigolo, D., Zhao, J., Handschin, S., Cao, X., DeMello, A. J., & Mezzenga, R. (2017). Continuous isotropic-nematic transition in amyloid fibril suspensions driven by thermophoresis. *Scientific Reports, 7*, 1211. https://doi.org/10.1038/s41598-017-01287-1

Walkinshaw, M. D., & Arnott, S. (1981). Conformations and interactions of pectins II. Models for junction zones in pectinic acid and calcium pectate gels. *Journal of Molecular Biology, 153*(4), 1075–1085. https://doi.org/10.1016/0022-2836(81)90468-X

Wang, Y., Shang, L., Zhao, Y., & Sun, L. (2022). Microfluidic generation of multicomponent soft biomaterials. *Engineering, 13*, 128–143. https://doi.org/10.1016/j.eng.2021.02.026

Ward, I. M. (Ed.). (2012). *Developments in oriented polymers—2*. Springer Science & Business Media. https://doi.org/10.1007/978-94-009-3427-6.

Wegst, U. G. K., Bai, H., Saiz, E., Tomsia, A. P., & Ritchie, R. O. (2015). Bioinspired structural materials. *Nature Materials, 14*(1), 23–36. https://doi.org/10.1038/nmat4089

Wei, G., Su, Z., Reynolds, N. P., Arosio, P., Hamley, I. W., Gazit, E., & Mezzenga, R. (2017). Self-assembling peptide and protein amyloids: From structure to tailored function in nanotechnology. *Chemical Society Reviews, 46*(15), 4661–4708. https://doi.org/10.1039/c6cs00542j

Xu, P., Xie, R., Liu, Y., Luo, G., Ding, M., & Liang, Q. (2017). Bioinspired microfibers with embedded perfusable helical channels. *Advanced Materials, 29*(34), Article 1701664. https://doi.org/10.1002/adma.201701664

Ye, X., Capezza, A. J., Davoodi, S., Wei, X. F., Andersson, R. L., Chumakov, A., Roth, S. V., Langton, M., Lundell, F., Hedenqvist, M. S., & Lendel, C. (2022). Robust assembly of cross-linked protein nanofibrils into hierarchically structured microfibers. *ACS Nano, 16*(8), 12471–12479. https://doi.org/10.1021/acsnano.2c03790

Yu, Y., Fu, F., Shang, L., Cheng, Y., Gu, Z., & Zhao, Y. (2017). Bioinspired helical microfibers from microfluidics. *Advanced Materials, 29*(18), Article 1605765. https://doi.org/10.1002/adma.201605765

Zhang, X., Min, B. G., & Kumar, S. (2003). Solution spinning and characterization of poly (vinyl alcohol)/soybean protein blend fibers. *Journal of Applied Polymer Science, 90*(3), 716–721. https://doi.org/10.1002/app.12699

Zhou, J., Xu, X., Xin, Y., & Lubineau, G. (2018). Coaxial thermoplastic elastomer-wrapped carbon nanotube fibers for deformable and wearable strain sensors. *Advanced Functional Materials, 28*(16), Article 1705591. https://doi.org/10.1002/adfm.201705591